# Transformation and Twinning Induced Plasticity in Metastable Ti-Mo Alloys under High Strain Rate Deformation

July 25, 2022

Authors: B. Ellyson[a*], K. Fezzaa[b], T. Sun[b1], N. Parab[b], A. Saville[a], C. Finfrock[a], C.J. Rietema[a2], D. Smith[a], J. Copley[a], C. Johnson[a], C.G. Becker[a], J. Klemm-Toole[a], C. Kirk[c], N. Kedir[d], J. Gao[c], W. Chen[c,d], R. Banerjee[e], K.D. Clarke[a] A.J. Clarke[a]

[a] George S. Ansell Department of Metallurgical and Materials Engineering, Colorado School of Mines, Golden, Colorado, [b] The Advanced Photon Source, Argonne National Laboratory, Lemont, Illinois, [c] School of Aeronautics and Astronautics engineering, Purdue University, West-Lafayette, Indiana, [d] School of Advanced Materials Engineering, Purdue University, West-Lafayette, Indiana, [e] Department of Materials Science and Engineering, University of North Texas, Denton, Texas

[*] Corresponding author

[1]Current affiliation: University of Virginia
[2]Current affiliation: Lawrence-Livermore National Laboratory

# 1 Abstract

The development of metastable titanium (Ti) alloys provides an unprecedented opportunity to expand their use in plasticity and damage critical applications like protective structures. However, such applications require knowledge of quasi-static to dynamic mechanical behavior, which is currently lacking. Here we perform in-situ, ultrafast synchrotron x-ray diffraction during high strain rate (Kolsky) pressure bar testing in tension and post-mortem electron microscopy to study TRansformation Induced Plasticity (TRIP) and TWinning Induced Plasticity (TWIP) in metastable Ti-Mo alloys. Two alloys, namely Ti-12Mo and Ti-15Mo (wt.%), were selected for study having different $\beta$-phase chemical stabilities. TWIP was observed in both Ti-12Mo and Ti-15Mo by in-situ synchrotron diffraction during high strain rate testing. Post-mortem microstructural characterization also revealed the presence of TRIP in Ti-12Mo. TWIP in Ti-15Mo was found to under-perform in terms of total elongation compared to TRIP/TWIP in Ti-12Mo. Ti-12Mo exhibited an average elongation of 17% compared to only 12% for Ti-15Mo with deformation at 1000 $s^{-1}$. TRIP resulted in significantly finer microstructure evolution and alleviated local strain accumulations in Ti-12Mo, suggesting TRIP can be used to tune available strength/ductility combinations in metastable Ti alloys under high strain rate deformation conditions.

# 2 Introduction

Ti alloys have been widely used in structural components in aerospace applications, due to their high strength to weight ratios. Recently, interest in a novel class of Ti alloys, namely metastable $\beta$ alloys, has been increasing, due to promising work hardening and ductility behaviors [1, 2, 3, 4]. Metastable $\beta$ Ti alloys have long been known to exhibit microstructure evolution during quasi-static deformation [5]. Only recently has the propensity for TRansformation Induced Plasticity (TRIP) and Twinning Induced Plasticity (TWIP) been studied with the aim of exploiting these

mechanisms to achieve desirable strength/ductility combinations by engineered work hardening response [6]. A similar approach has been successfully used to develop a myriad of useful advanced high strength steels for automotive applications, driven by the need for lightweighting and improved crash performance [7, 8]. Metastable TRIP/TWIP Ti alloys may similarly open the door to mechanical property combinations for the aerospace and defense sectors. For strong, ductile and tough metastable Ti alloys to become ubiquitous, however, understanding TRIP and TWIP and the effect of strain rate, temperature, and strain path are crucial.

Recent publications have highlighted that TRIP in Ti alloys is less favorable for obtaining higher yield stresses compared to TWIP for quasi-static tensile deformation [4, 9, 10]. On the other hand, TRIP has been revealed as a powerful mechanism for internal stress relaxation, specifically where twin/twin interactions occur [4] and at twin and secondary phase boundary interactions [9] where local stresses may be high. Nevertheless, the trend seems to be moving toward TWIP-dominant alloys, based upon our current understanding [3, 4, 11] from quasi-static mechanical testing and microstructure characterization. For the broader use of metastable Ti alloys to become a reality, specifically in applications requiring substantial plasticity or damage tolerance, quasi-static mechanical behavior may be a misleading experimental basis for alloy and microstructure design, given that plasticity and fracture are inherently dynamic processes in real-world scenarios. This implies the dynamic behavior of TRIP/TWIP alloys needs to be well-understood, especially if they are to be utilized in crash or blast resistant scenarios where energy absorption is essential. In cases such as these, there are no substitutes for high strain rate experiments.

Only a few high strain rate deformation studies have been published to date on metastable $\beta$ Ti alloys, mostly concentrating on the strain rate sensitivity from quasi-static strain rates up to the low end of intermediate strain rates ($10^{-5}$ to $10^{-1}$ $s^{-1}$) [12, 13, 14]. While the data presented in these studies are useful, they

do not extrapolate to high strain rate behaviors because different mechanisms like dislocation generation and motion may dominate in different strain rate regimes [15]; in addition temperature effects (i.e., adiabatic heating), pathway dependent microstructure evolution is also not well understood. Ahmed et al. [12] have published one of the only studies where strain rates up to $10^2$ $s^{-1}$ were tested on an $\alpha+\beta$ TRIP/TWIP Ti-10V-3Fe-3Al (wt. %) alloy. While their study was performed in compression, they concluded that TWIP was dominant over TRIP as strain rate increased, although all mechanisms were found to be active over the entire strain rate range regime studied (i.e., no TRIP suppression occurred). To the authors' knowledge, only two studies have looked at metastable $\beta$ Ti alloys [16, 17] deformed at strain rates on the order of $10^3$ $s^{-1}$ and only in compression. Both studies found evidence of TRIP and TWIP in the deformed state; increased work hardening was provided by both mechanisms. Specifically, Yang et al.'s study on Ti-8.5Cr-1.5Sn (wt. %) [16] showed that TRIP and TWIP are a powerful deterrent to the formation of adiabatic shear bands. To date, no studies have systematically compared different alloys and chemical phase stabilities under high strain rate deformation conditions, which controls the microstructure evolution.

Here we investigate the microstructure evolution in two Ti-Mo alloys with different $\beta$-phase chemical stabilities using ultrafast synchrotron x-ray diffraction during high strain rate tensile deformation. Complementary post-mortem electron microscopy was also performed. **These results reveal the importance of TRIP in maintaining higher elongations, and thus the potential for energy absorption, and suggest that TRIP-capable alloys (Ti-12Mo) out-perform TWIP alloys (Ti-15Mo) at high strain rates, due to the central role that martensite plays in local stress relaxation.**

# 3 Methodology

## 3.1 Ultrafast Synchrotron X-Ray Imaging and Diffraction during High Strain Rate Deformation

Modified (Kolsky) pressure bar testing together with high brilliance, high-flux, ultrafast synchrotron x-ray imaging and diffraction was performed at sector 32-ID-B at the Advanced Photon Source (APS) at Argonne National Laboratory (ANL). The details of the modified (Kolsky) pressure bar apparatus have been reported elsewhere [18, 19, 20]. A schematic of the experimental setup is shown in Figure 1 a), which provides the simultaneous capture of x-ray imaging, diffraction and mechanical test data. A Photron FASTCAM SA-Z type 2100K-M-64G camera using a LuAG:Ce scintillator (100 thick) and a 10X microscope objective (Mitutoyo long WD) at a frame rate of 50400 frames per second (fps) was used for imaging. Diffraction data were captured in full transmission geometry with a Shimadzu HPV-X2, coupled to an image intensifier and an LSO:Ce scintillator (300 thick), at a frame rate of 298507 fps. The mechanical test data were acquired with an oscilloscope at an acquisition rate of $10^8$ Hz. For the x-ray setup, an undulator gap of 12 $mm$ was used, providing a "pink-beam"-like condition with a maximum flux at a wavelength of 0.512 Å and a characteristic, asymmetric intensity profile around the harmonic energies, with a tail dropping off in intensity gradually toward the lower energies. A beam size of 2 $mm$ wide by 1 $mm$ in height was used to illuminate the gauge length of each tensile specimen. This large beam size, combined with the tail of the energy profile, lead to significant instrument and source broadening of the diffraction peaks, as discussed in the supplementary materials. The detector-to-sample distance was roughly 0.6 m, and the resulting pixel size was roughly 32 $\mu m$ on the detector. Different detector positions were used to obtain different resolutions and q-space ranges. The sample geometry is also provided in Figure 1b.

Standards of pure Al and pure Ta foil were used to calibrate the detector position.

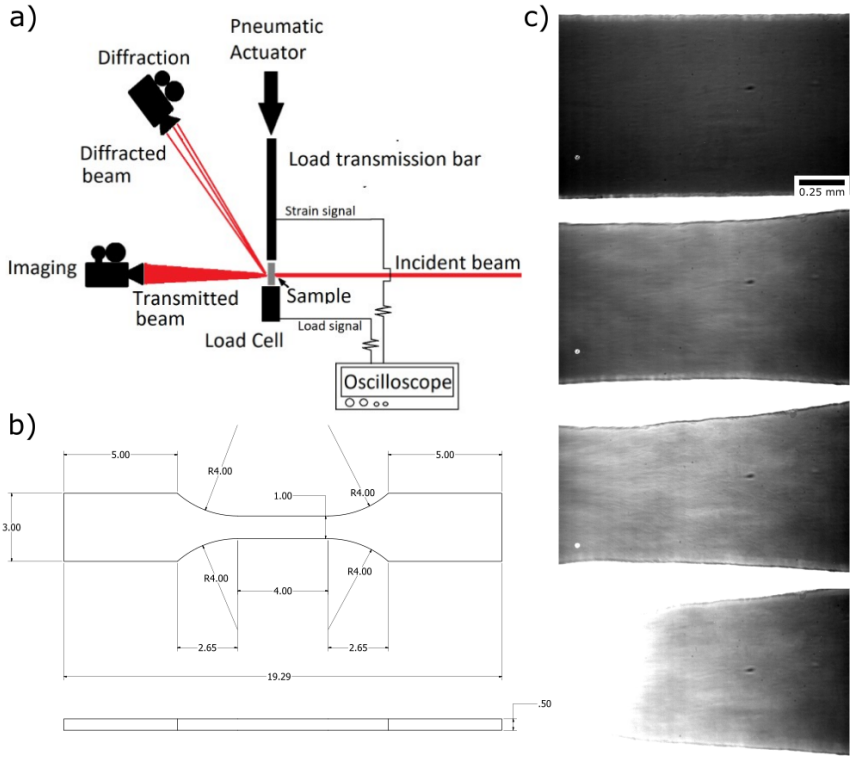


**Figure 1:** a) Schematic of the modified (Kolsky) pressure bar setup at the APS at ANL. b) Tensile test geometry used in this work (dimensions in mm). c) Example synchrotron x-ray radiographs obtained during tensile deformation, showing necking and fracture in the gauge length. This specimen was deformed at a strain rate of $10^3$ $s^{-1}$. The observed contrast is associated with microstructure evolution.

Analysis of the raw diffraction data was performed using High Speed Polychromatic Diffraction (HiSPoD), a MATLAB program developed at sector 32-ID. The details of the program and its implementation are provided elsewhere [21]. The program was used to calibrate the beam position and detector/sample geometry, allowing for the calculation of a q-space map (radial coordinates) for integration of the diffraction patterns.

The modified (Kolsky) pressure bar apparatus used strain gauges to capture the incident and reflected pulses. Due to space restrictions in the hutch, the load data were measured using a fast-response quartz load cell instead of a typical transmission bar. Measurements made during testing of a brittle ceramic indicated the decay time of the load signal was roughly 0.35 V/$\mu s$. In this study, strain rates of roughly $10^3$ and $2\times10^3$ $s^{-1}$ were achieved. Stress and strain data were averaged for all specimens

of each alloy by averaging the stress value of each replicate for each strain increment.

## 3.2 Sample Preparation, Post-Mortem Microstructure Characterization and Quasi-static and Intermediate Strain Rate Testing

The Ti-15Mo specimens for testing at the APS were machined from a 15.8 $mm$ diameter bar stock, whereas the Ti-12Mo specimens were wire electro-discharge machined from a rolled sheet. The flat specimens extracted from the round bar of the Ti-15Mo alloy likely exhibited slight variations in texture, due to the sample extraction strategy. In all cases, the specimens were ground to a final thickness of 0.5 $mm$ using 320 grit SiC metallographic paper. The tensile specimens were wrapped in Ta foil and encapsulated under vacuum in quartz tubes to minimize contamination and oxygen pick-up. Ti-12Mo specimens were held at 1093 K for 30 min. Ti-15Mo specimens were held at 1073 K for 30 min. All samples were immediately quenched into room temperature distilled water by breaking each quartz capsule. The resulting microstructures for both alloys was the $\beta$-phase with an equiaxed grain structure and average grain size of roughly 35 $\mu m$ for Ti-15Mo and 45 $\mu m$ for Ti-12Mo, as determined by Electron Backscatter Diffraction (EBSD). The details of the EBSD measurements are provided later in this section. With a total gauge thickness of 0.5 $mm$ and grain sizes in the range of 40 $\mu m$, we can assume that roughly 10 grains were present through thickness in each specimen. Additionally, it can be estimated that roughly $5 \times 10^4$ grains were in the gauge section, and only about half that number were illuminated by the beam. This number is considered a conservative upward-bound estimate, since a spherical grain shape was assumed, which leads to overestimating the number of grains present in a given volume.

Quasi-static tensile testing was performed at the Colorado School of Mines with an electromechanical Alliance load-frame at a strain rate of $10^{-3}$ $s^{-1}$ using a 1 in

Shepic type extensometer. Intermediate strain rate tests were performed on a hydraulic MTS load-frame using a 1 in MTS blade-type extensometer. All quasi-static and intermediate strain rate tests were performed using ASTM E8 standard [22] subsize geometry tensile specimens with a gauge length of 25.4 mm and a cross section of 3.175 mm by 6.35 mm.

An FEI Helios 600i dual-column Focused Ion Beam (FIB)/Field Emission Scanning Electron Microscope (FESEM) was used to make lift-outs for Transmission Electron Microscopy (TEM). TEM was performed in an FEI Talos F200X CTEM/STEM at 200 kV. EBSD specimens were prepared by electropolishing at 20 V and 253 K, using a mixture of 6 % perchloric and 4 % hydrochloric acids diluted with a 2 to 1 mixture of methanol and butoxyethanol. EBSD scans were performed in an FEI Helios 600i dual-column FIB/FESEM at an accelerating voltage of 20 kV with 11 nA of current. No post-scan clean-ups were performed.

# 4 Results

## 4.1 Mechanical Properties

### 4.1.1 Quasi-Static and Intermediate Strain Rate Mechanical Properties

Engineering stress versus engineering strain curves obtained from quasi-static ($10^{-3}$ $s^{-1}$) and intermediate ($10^{-1}$ $s^{-1}$) strain rate tests of Ti-15Mo are presented in Figure 2 a). A hundred fold increase in deformation rate leads to an increase in yield stress and reduction in total and uniform elongation (Figure 2 a) and b)). Figure 2 b) shows true stress versus true strain of Ti-15Mo and Ti-12Mo. Ti-12Mo has lower yield stress and overall strength at comparable strain levels, but greater uniform elongation and maximum work hardening rate (WHR) compared to Ti-15Mo. WHR was determined using the first derivative of the stress ($\frac{d\sigma}{d\varepsilon}$) and a running average over 50 points for smoothing. The main difference between the two alloys, apart

from composition, is the possible activation of TRIP in the Ti-12Mo alloy. TWIP was anticipated in Ti-15Mo, based upon phase stability. Composition likely plays a major role in the observed strength difference, as Mo is a potent solid solution strengthener in the $\beta$-phase of Ti [23]. The Ti-12Mo data shown in Figure 2 b) was chosen to reflect Ti-12Mo in the as-quenched, unaged state, where $\omega$-phase hasn't significantly altered the mechanical response [24].

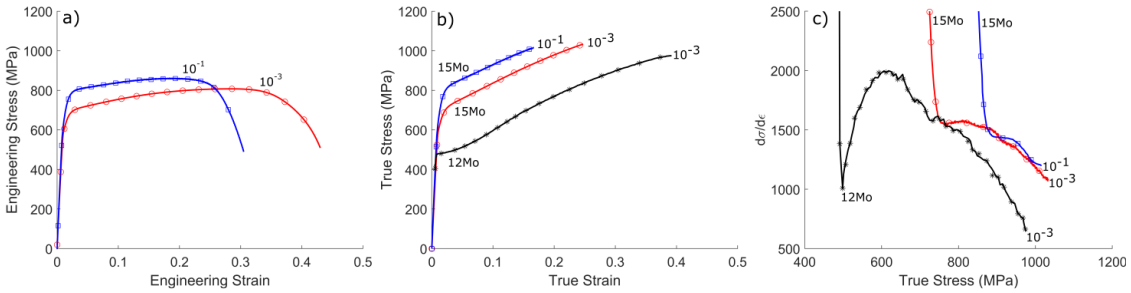


**Figure 2:** a) Engineering stress versus engineering strain curves for Ti-15Mo tested at quasi-static and intermediate strain rates of $10^{-3}$ and $10^{-1}$ $s^{-1}$. b) True stress versus true strain of Ti-15Mo and Ti-12Mo deformed in tension at a strain rate of $10^{-3}$ $s^{-1}$ and Ti-15Mo tested at an intermediate strain rate of $10^{-1}$ $s^{-1}$. c) Instantaneous WHR as a function of true stress for the three conditions shown in b). The data for Ti-12Mo was taken from [11].

The true stress versus true strain response of Ti-15Mo is also shown in Figure 2 b) for quasi-static and intermediate strain rates. Interestingly, the WHR seems to be comparable between the two strain rates. However, an apparent reduction in uniform elongation correlates with a concurrent reduction in work hardening as flow stress approaches the ultimate tensile strength (UTS) of 1 GPa. Figure 2 c) shows the substantial difference in WHR at high flow stresses exhibited by both alloys. TRIP-capable Ti-12Mo exhibits an overall larger WHR over a larger stress range, but does not reach Ti-15Mo equivalent stress levels. The superior flow stress exhibited by Ti-15Mo is most likely due to the Mo solid solution strengthening in the matrix. When quasi-static and intermediate strain rates are considered for Ti-15Mo, it is clear that the WHR is similar for a given stress level after yielding. The work hardening behavior of Ti-15Mo does not appear to be strongly sensitive to strain rate. This finding supports the claim that plastic strain is mostly mediated

by dislocations, while work hardening is controlled by slip and twinning. This is discussed further later.

### 4.1.2 High Strain Rate Mechanical Properties

Figure 3 a) shows engineering stress versus engineering strain curves obtained from tensile testing of Ti-12Mo with the modified (Kolsky) pressure bar setup at the APS at ANL. Due to the inherent variability associated with these small scale, high strain rate tests, averaging of the curves was performed to obtain representative behavior. Two different strain rates were achieved during testing, roughly $10^3$ and $2 \times 10^3$ $s^{-1}$. The difference between the two strain rates for the Ti-12Mo alloy is evident in Figure 3 a).

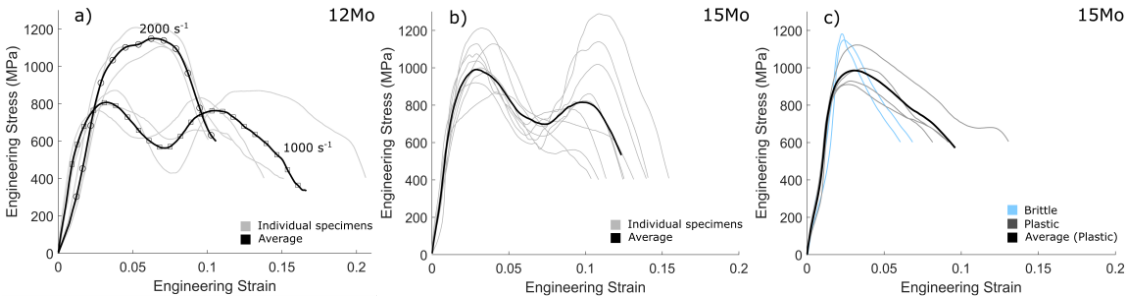


**Figure 3:** a) Engineering stress versus engineering strain curves for Ti-12Mo. The full black curves with symbols represent the average behavior of 5-10 tests, depending on alloy and strain rate. The stress-strain curves of individual specimens used in the average are shown in grey. b) Engineering stress versus engineering strain curves of Ti-15Mo deformed in tension at a strain rate of roughly $10^3$ $s^{-1}$. Individual specimens are shown in grey, and the average behavior is shown in black. c) Engineering stress versus engineering strain curves of Ti-15Mo deformed at $2 \times 10^3$ $s^{-1}$. Curves in light blue represent outliers that exhibited no macroscopic ductility or "brittle" behavior, and were not used in the calculated average response shown in c).

Due to the inherently noisy nature of the high strain rate mechanical testing data, it is impossible to identify an exact uniform elongation and WHR. Even the exact moment of failure is hard to pinpoint, in large part due to the decay time of the load cell signal. To circumvent this difficulty, a cutoff stress equal to half the maximum stress was chosen as a comparative value for elongation (Figure 3). Sur-

prisingly, even at the highest strain rate, Ti-12Mo still exhibits measurable ductility. The increase in flow stress exhibited between $10^3$ $s^{-1}$ and $2 \times 10^3$ $s^{-1}$ is indicative of the alloy resisting localization.

Figures 3 b) and c) show engineering stress versus engineering strain curves for Ti-15Mo samples tested with the modified (Kolsky) pressure bar setup at strain rates of $10^3$ $s^{-1}$ and $2 \times 10^3$ $s^{-1}$. Figure 3 b) shows individual test specimen results in light grey in the background; the average behavior is indicated in black. The ductility and maximum stress vary amongst the individual test specimens at this strain rate, with total elongation (cutoff stress set at 400 MPa) varying between 0.1 and 0.16. The variability in total elongation and maximum stress exhibited by these specimens is, in part, due to slight variations in texture in the specimens mentioned above. Another source of variability is the similarity between grain size and sample thickness, i.e., only a few grains are present through thickness.

Curves for individual specimens of the Ti-15Mo alloy tested at the highest strain rate of $2 \times 10^3$ $s^{-1}$ were divided into 2 categories, as the mechanical behavior diverged greatly. Specimens either exhibited limited ductility, or none at all, i.e., fracture occurred before any plastic deformation could be measured. The latter are labeled in light blue as "brittle" in Figure 3 c). Other specimens that exhibited macroscopic plasticity were labeled as "plastic", and are represented in grey. They were used to calculate the average curve shown in black. When comparing these data with those collected at $10^3$ $s^{-1}$, the yield stress is roughly equal, while elongation is decreased. This behavior is indicative of having reached a strain rate at which localization is consistently present at low plastic strain.

## 4.2 Ultrafast Synchrotron X-Ray Imaging and Diffraction during High Strain Rate Testing in Tension

In-situ synchrotron x-ray diffraction data is presented for Ti-15Mo and Ti-12Mo in Figure 4. In both cases, raw diffraction frames and integrated diffraction patterns show clear evidence of grain refinement during deformation and texture evolution. In Figure 4 a) and b), the first raw diffraction frames show large diffraction spots distributed radially, mostly centered around 4 $nm^{-1}$ and 2.7 $nm^{-1}$ in q-space. These spots are the result of the initially large grain sizes in both alloys. As plasticity evolves, the spots can be seen turning into full rings of diffuse intensity. The diffraction signal is a clear indication of microstructural evolution, leading to refinement of the average size and change in orientation of the diffracting domains. The refinement and re-orientation causes the diffracted photons to be more evenly distributed in the $\phi$, or azimuthal, direction on average. Secondly, the texture component of the diffraction can also be seen to evolve. Figure 4 c) and d) show an integrated diffraction pattern as a function of engineering strain, where an integrated line-out for each frame is calculated and stacked to form a heat map. It can be clearly seen that the maximum intensity, which centers around 18° in $2\theta$ space (or roughly 4 $nm^{-1}$ in q-space), rapidly shifts to form an increasing maximum near 12° (or roughly 2.7 $nm^{-1}$ in q-space). These positions correspond to the $\{200\}_\beta$ and $\{110\}_\beta$ peaks, respectively. The change in maximum intensity is indicative of a texture change during deformation.

Possible explanations for this type of diffraction signal fall into two categories, namely: 1) sub-grain formation and 2) deformation twinning. Theoretically, when dislocation slip is active, cells eventually form, which upon further plastic straining, evolve into sub-grains. Further slip tends to cause a rotation of the grains relative to the tensile axis, such that the slip planes move toward a low Schmid Factor (SF), normally developing a {110} type texture parallel to the tensile axis in BCC crystals. On the other hand, deformation twinning will also lead to the same type

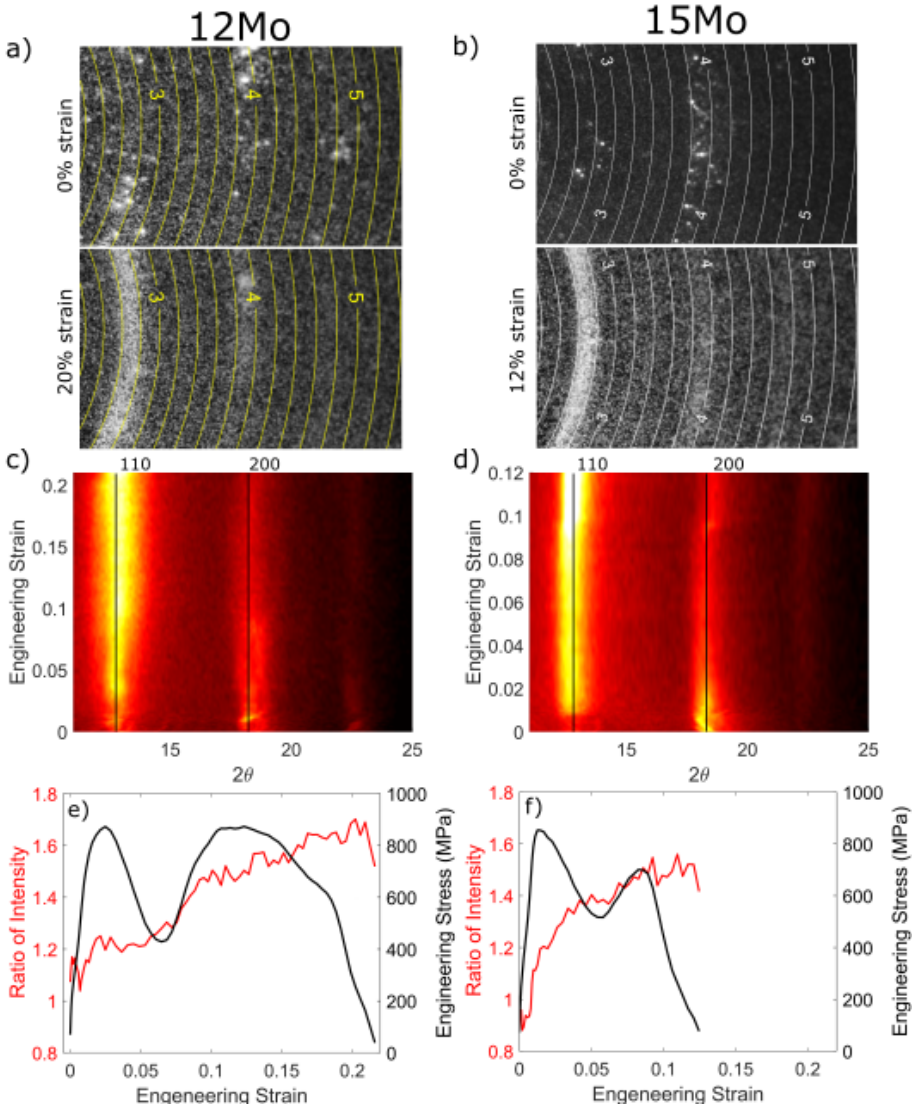


**Figure 4:** In-situ synchrotron x-ray diffraction during high rate tension testing. Raw diffraction frames showing the evolution from partial rings populated by spots to full diffuse rings in a) Ti-12Mo and b) Ti-15Mo The white circular lines indicate contours of constant q, with 3, 4 and 5 $nm^{-1}$ labeled and the equivalent strain is indicated next to the frame. Integrated diffraction pattern as a function of engineering strain for c) Ti-12Mo and d) Ti-15Mo. Black vertical lines indicate the theoretical position of $\beta$ phase reflections and are labeled at the top of the map. Ratio of integrated intensity of the $\{110\}_\beta$ peak and the integrated intensity of $\{200\}_\beta$ peak shown in red on the left axis and engineering stress shown in black on the right axis, both as a function of engineering strain.

of "bulk-averaged" microstructure evolution and diffraction contrast. Indeed, the formation of a twin during plastic straining is the result of local re-orientation of a sub-volume within a grain to a specific twin relation. This process accumulated many times within a grain and over many 100s of grains will lead to a spots-to-ring type of diffraction signal, as shown. Due to the orientation dependence of deformation twinning during TWIP, a preferential texture may also evolve [25, 26]. In

summary, both alloys exhibit strong evidence of microstructural evolution, particularly grain refinement of the $\beta$-phase matrix.

In both integrated diffraction patterns presented in Figure 4 c) and d), intensity near the $\{110\}_\beta$ reflection becomes dominant over a large portion of the deformation. This indicates that plasticity is preferentially rotating the $\{110\}_\beta$ planes into the Bragg condition at the expense of others. No evidence of phase transformation was found for Ti-15Mo. Unfortunately, signs of deformation-induced phase transformation are not readily discernible in the diffraction data shown for Ti-12Mo. However, post-mortem characterization proves significant transformation occurred during deformation in Ti-12Mo, as shown in Figure 6, while it is completely absent in Ti-15Mo (Figure 13). Ti-12Mo forms a martensitic phase that is only a slight symmetry breakdown of the BCC $\beta$ phase. As such, many diffraction peaks (especially those of highest intensity) either overlap or are very close to the $\beta$ phase peaks in the region of the $\{110\}_\beta$ reflection. It is almost certain that the measured intensity for Ti-12Mo, as shown in Figure 4 a) and c), includes contributions from both phases, at least near the $\{110\}_\beta$ position. It should be noted that unequivocal evidence of transformation is not captured by the in-situ diffraction data, most likely due to angular resolution and dynamic intensity range limitations.

Figure 4 e) and f) show the ratio of the integrated intensity of the $\{110\}_\beta$ position and the integrated intensity of $\{200\}_\beta$ position, as well as engineering stress, as a function of engineering strain. The ratio of integrated intensities provides a visual indication of the rate at which texture evolves as a function of strain. It is interesting to note that the ratio gradually increases from the onset of loading up to fracture in Ti-12Mo. When compared to the engineering stress response, the gradual increase in ratio of intensities correlates with a high strain to fracture and nearly-constant flow stress (disregarding the load oscillation caused by ringing in the sample). This contrasts strongly with the sharp initial increase exhibited by Ti-15Mo up to an

engineering strain of roughly 0.05, followed by a significant decrease in the slope from 0.05 to 0.12, where fracture occurs. The noted slow-down in texture evolution exhibited by the Ti-15Mo specimen also correlates with a decrease in the load response and lower strain to fracture, as compared to the Ti-12Mo specimen. These data appear to indicate that slower overall rate of microstructural evolution in the Ti-12Mo alloy allows for higher plastic strains to be reached before fracture occurs.

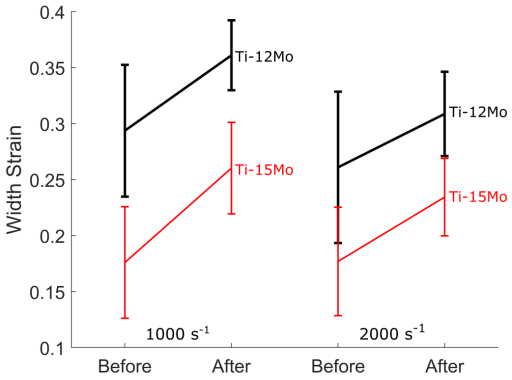


**Figure 5:** Comparison of the reduction in gauge section width taken from synchrotron x-ray imaging data. The average and standard deviation of the gauge section width at the narrowest point is shown in the last frame before fracture (Before) and after fracture (After) for both alloys tested at two strain rates (1000 and 2000 $s^{-1}$). Measurements were only included for samples where the entire width of the fractured gauge length was visible. When possible, measurements from both sides were averaged for a single specimen.

To help supplement the mechanical test data, synchrotron x-ray imaging data were used to measure and calculate reduction in area, or an approximate thereof (Figure 5). The radiography images allowed for the measurement of the reduction of the width of the gauge section, up to the moment of fracture, and the resulting fractured halves. Figure 5 shows the average (and standard deviation) of each alloy for both strain rates achieved during the in-situ experiments. The measurements indicated as "Before" were measured from the last frame, where the specimen is seen whole, whereas the measurements labeled "After" were obtained from a frame after fracture occurred. The average and error bars support the statement that Ti-12Mo exhibits higher ductility up to fracture at both $10^3$ and $2 \times 10^3$ $s^{-1}$.

## 4.3 Post-mortem Microstructure Characterization

The in-situ synchrotron x-ray diffraction data provide insights into the microstructure evolution that occurs during deformation. However, post-mortem characterization is necessary to understand the exact nature of the evolution, since diffraction is fundamentally a volume averaged technique. As such, fractured specimens from both alloys were characterized using EBSD and TEM to obtain important information about the fine-scale structural evolution.

### 4.3.1 TRIP/TWIP Ti-12Mo

Evidence of $\beta$-phase deformation twinning and transformation are present in the microstructure of deformed Ti-12Mo. Large deformation bands can be seen traversing grain boundaries with little re-orientation, plausibly due to accommodation in the neighboring grains [27, 28]. Figures 6 a) and b) show an IPF + IQ and Phase + IQ maps, respectively, of an EBSD scan where complex microstructure evolution can be seen, along with strong evidence of deformation twinning as the primary deformation product. Figure 6 c) shows an IQ map overlaid with $\{332\} < 113 >$ twin boundaries. This map shows clear evidence of the concurrent presence of transformation and twinning in the deformed state, similar to the microstructure evolution reported for quasi-static deformation [1, 11]. Secondary twinning can also be seen to further sub-divide the $\beta$-phase matrix remaining between the primary twins in one of the grains on the left side of the map (indicated by the red box in Figure 6 c). Between the two black lines in Figures 6 b) and c) is the transition from untransformed primary twins in the bottom right to twins containing secondary transformation product, i.e. martensite in the upper portion of the same twinned laths. This is clear experimental evidence of secondary transformation within the primary twin accommodating further plastic deformation within the initially twinned crystal.

The bands contain more complex substructure that is too fine to be properly

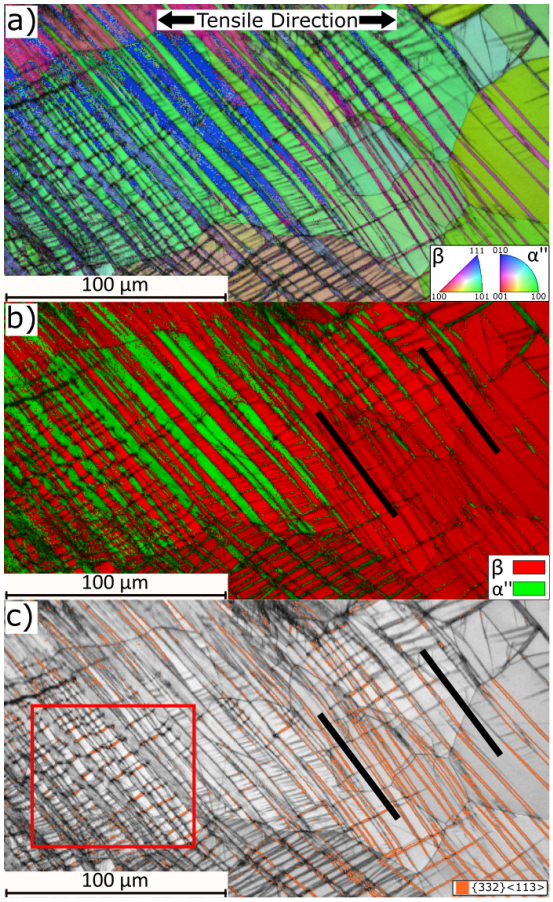


**Figure 6:** EBSD of a Ti-12Mo specimen deformed in tension at a strain rate of $10^3$ $s^{-1}$ taken outside the necked region of the gauge length. a) IPF + IQ map and b) Phase + IQ map c) IQ map with twin boundary overlay; orange represents $\{332\} < 113 >$ twin boundaries. The phase map shown in b) clearly indicates the presence of martensite in the large bands traversing the grains, while the IQ map shown in c) shows the presence of $\{332\} < 113 >$ twins. The red box highlights secondary twinning. The black lines in b) and c) highlights the transitions of primary twins forming internal secondary martensite. This EBSD scan shows how primary bands seemingly formed first as deformation twins, with subsequent internal transformation to martensite.

characterized by EBSD alone. A FIB liftout was produced to contain a cross section of one of these bands. Figure 7 shows the results of TEM characterization of one of these bands. The band exhibited a total of five of the six possible $\alpha$" variants, along with residual $\beta$-phase. Figures 7 b) through c) show Selected Area Diffraction Patterns (SADPs) taken from the same tilting condition that clearly show the relation between the $\beta$ phase (Figures 7 b) and c)) and at least 2 of the martensite variants (Figures 7 c) and d)). Three other variants were also indexed using SADPs taken in other locations within this band, but are not shown here for conciseness. Figure 7 h) shows a centered dark field (DF) image taken using contributions from two different

martensite variants ($\{112\}_{\alpha''}$ and $\{200\}_{\alpha''}$), highlighting the complex sub-structure and distribution of martensite in this band. The level of microstructure evolution and locally accumulated plastic strain is such that partial rings and "smeared" spots were measured in Figure 7 g), which is indicative of high local misorientation and fine crystallite sizes.

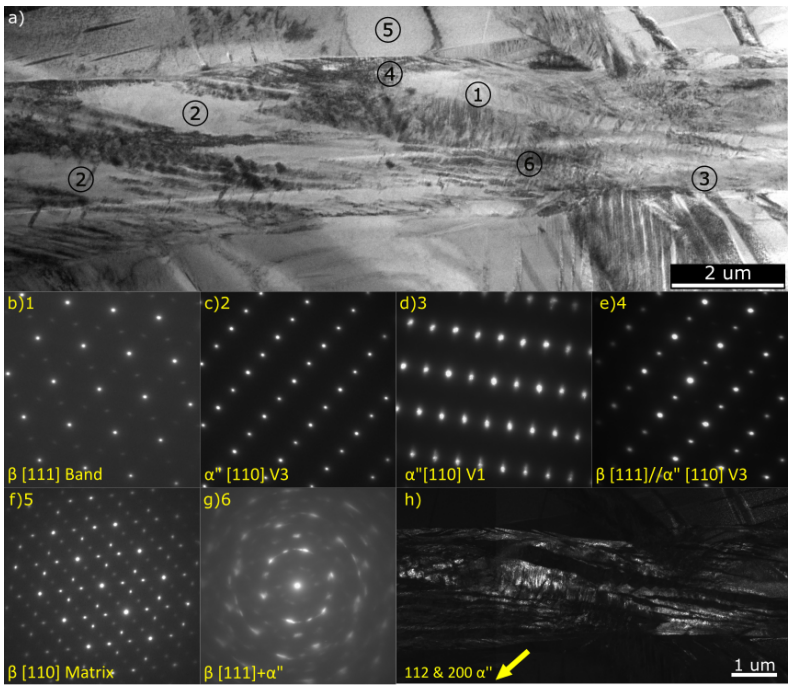


**Figure 7:** TEM of a large primary deformation band. a) Bright Field (BF) overview of the band with the location of selected area diffraction patterns (SADPs) taken in the same tilt condition indicated by the numbered circles (b-e). b) SADP of the $\beta$ phase matrix taken parallel to the $[111]_{\beta}$ Zone Axis (ZA). c) SADP of martensite taken down the $[110]_{\alpha"}$ ZA. d) SADP of martensite taken down the $[110]_{\alpha"}$ ZA d) SADP containing patterns from both the $\beta$ phase matrix taken parallel to the $[111]_{\beta}$ ZA and of martensite taken down the $[110]_{\alpha"}$ ZA, as shown in d), highlighting the orientation relationship between the matrix and the martensite. f) SADP taken in the $\beta$ phase of the grain, outside the main band and parallel to the $[110]_{\beta}$ ZA of the $\beta$ phase. g) SADP of a region exhibiting fine sub-structure, composed of multiple variants of martensite, along with the $[111]_{\beta}$ ZA of the band. h) Two-beam dark field (DF) image taken using contributions from two different martensite variants. G-vectors used to form the image are indicated on the image.

Evidence of secondary and tertiary transformation product is also present in the matrix of the Ti-12Mo alloy. Figure 6 shows some of the secondary product to be $\{332\} < 113 >$ deformation twins. Secondary twinning and subsequent internal secondary transformation are also activated. Interestingly, TEM also reveals that secondary transformation is activated in the matrix, once primary twinning has

already subdivided the grains. Figure 8 a) shows a bright field (BF) overview of secondary transformation in the matrix; this image was taken in the tilt condition used to produce to the SADP shown in Figure 8 b). It can be seen that the matrix of the grain and the smaller laths are down zone, showing dark contrast and signifying the smaller laths are contributing the SADP shown in Figure 8 b). Figures 8 c) through f) further support this, as the DF and BF images clearly show the smaller laths belong to the phase contributing to this pattern. It should be noted that contrast is obtained from the matrix in the DF images, due to overlap with the $\omega$ phase reflection of the matrix, as seen in Figure 8 b). The $\omega$ phase is known to be present in the $\beta$-phase matrix of Ti-12Mo [24]. These TEM images strongly support the fact that martensite laths formed directly from the $\beta$-phase matrix, not within a $\beta$ twin.

### 4.3.2 TWIP Ti-15Mo

Figure 9 a) shows an IPF map of an EBSD scan taken from the gauge section of a Ti-15Mo specimen deformed in tension at a strain rate of roughly $10^3$ $s^{-1}$. The IPF map shows a significant amount of microstructure evolution occurred during deformation. Large deformation product can be seen traversing the grains, and, in some instances, traversing multiple grains. These lath-like features have been identified as twins. This type of accommodative twinning crossing grain boundaries has been reported before in Ti-15Mo after quasi-static strain rate testing [27, 28]. Indeed, Figure 9 b) shows an IQ map of the same scan, but with twinning boundaries overlaid in color, showing the majority of twins indexed are of the $\{332\} < 113 >$ type, equivalent to $\Sigma 11$ coincident site lattice (CSL) boundaries. All primary twins indexed are $\{332\} < 113 >$ type.

Misorientation line profiles across twin boundaries further confirm this finding, as the characteristic $\Sigma 11$ misorientation of $50.5°$ about the $[110]_\beta$ is found. Two

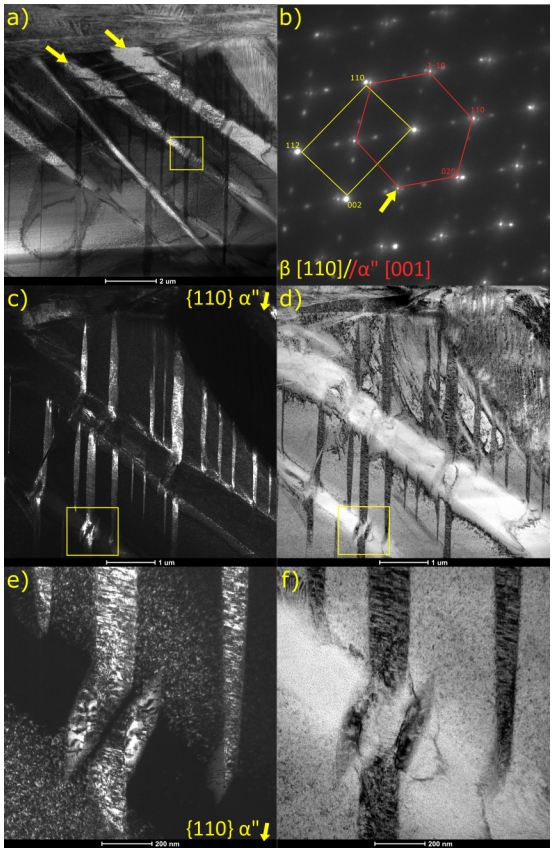


**Figure 8:** TEM of secondary transformation product in Ti-12Mo deformed in tension at a rate of $10^3$ $s^{-1}$. a) BF image showing an overview of the characterized zone. The arrows indicate two martensite laths that visibly traverse another variant, as shown in c-f). b) SADP of the matrix and the laths that appear dark in a), taken parallel to the $[110]_\beta$ ZA of the $\beta$ phase. This SADP was taken in the same tilt condition as the BF image shown in a). c-f) A DF and BF image pair taken using the reflections indicated by an arrow in b). c) and d) are a DF and BF image pair, respectively, highlighting the distribution of the martensite variant indexed in b). e) and f) are a DF and BF image pair, respectively, showing an expanded view of the region highlighted in c) and d). The same region is highlighted in a), for clarity. These images clearly show the first variant of martensite (indicated in a), shearing the illuminated martensite laths.

examples are presented in Figures 9 c) and f), with corresponding insets numbered 1 and 2 in a) and line-profiles shown in d) and e), respectively. Specifically, it can be seen in Figure 9 d) that the larger twins present internal or secondary twinning also of the $\{332\} < 113 >$ type. Interestingly, some of the boundaries are also identified as $\{112\} < 111 >$ twin boundaries, equivalent to $\Sigma 3$ CSL boundaries. Figure 9 d) indicates the presence of secondary twinning in a twinned grain, which is further discussed in the supplementary materials.

Interestingly, the area fraction of twins is significantly lower in the high strain

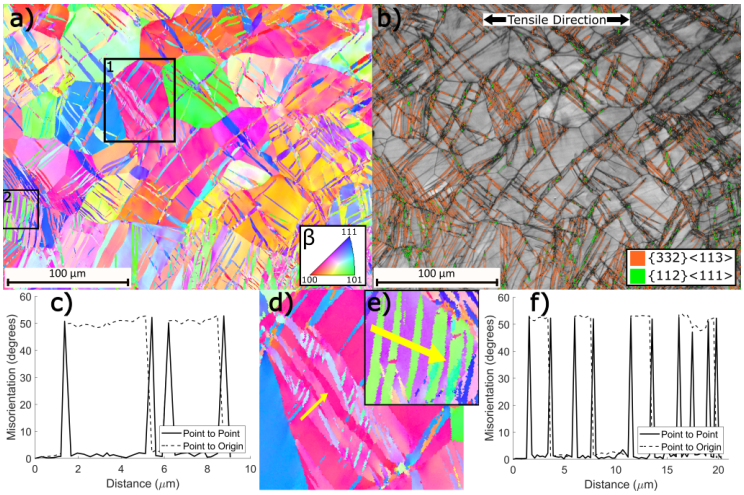


**Figure 9:** Evidence of primary twinning in an EBSD scan of a Ti-15Mo sample deformed in tension at a strain rate of $10^3$ $s^{-1}$. This scan was taken in the gauge near the necked area. a) An IPF map. The areas highlighted by the black boxes numbered 1 and 2 are presented as insets in d) and e), respectively. b) An IQ map with twin boundaries overlaid: orange represents $\{332\} < 113 >$ twin boundaries, while green represents $\{112\} < 111 >$ twin boundaries. c) The misorientation profile taken along the yellow arrow indicated in d) (corresponding to the inset numbered 1 in a)). f) The misorientation profile taken along the yellow arrow indicated in e) (corresponding to the inset numbered 2 in a).

rate deformation condition than after deformation at quasi-static strain rates. Studies on Ti-15Mo by Min et al. [29, 30] show the area fraction of twins is roughly 0.5 on average, and is up to 0.8 in favorably oriented grains. However, the EBSD scans shown here after high strain rate deformation reveal the twin area fraction, measured to be 0.13, is substantially lower compared to after quasi-static strain rate deformation [27], most likely due to lower plastic strain levels reached before fracture. This implies that TWIP is less active as strain rate increases in Ti-15Mo. In-situ deformation studies [30] reveal this is most likely due to $\{332\} < 113 >$ twins being formed as a function of strain, specifically in preferably oriented grains, and not stress within grains. If this is true and twinning is active over a smaller plastic strain range at higher strain rates, it would lead to a lower twin fraction, even if comparable stress levels were reached. The high strain rate ductility is substantially lower than after quasi-static strain rate testing. While the fundamental dependency is still unclear, the data presented here support this trend. This may have significant implications for the usefulness of TWIP Ti alloys for high strain rate applications.

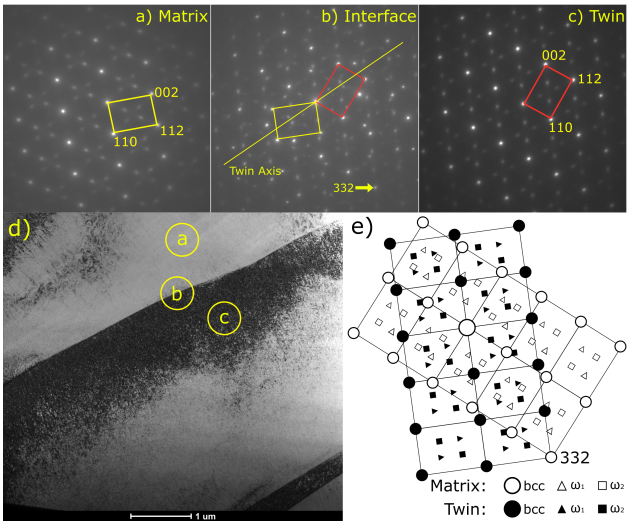


**Figure 10:** TEM of a $\{332\} < 113 >$ twin interface taken from the gauge section of a TWIP Ti-15Mo specimen deformed in tension at $10^3$ $s^{-1}$. a) SADP pattern of the matrix down the $[110]_\beta$ ZA. The $\beta$ phase matrix reflections are labeled in the first Brillouin zone. The projected reciprocal unit cell is outlined for clarity. b) SADP pattern of the twin/matrix interface looking down the $[110]_\beta$ ZA of both crystals. The projected reciprocal unit cell is outlined for the twin and matrix crystal, as well as the twinning axis. The twinning plane is also labeled. c) SADP pattern of the twin looking down the $[110]_\beta$ ZA. The $\beta$ phase matrix reflections are labeled in the first Brillouin zone. The projected reciprocal unit cell is outlined for clarity. d) A two-beam bright field image taken using the g=$110_\beta$ diffraction condition. The position where the patterns in a), b) and c) were taken is indicated in d). e) Schematic providing the key to interpreting the diffraction pattern shown in b).

To provide further proof of the nature of the deformation twins found in Ti-15Mo samples, TEM characterization was conducted on a FIB liftout taken at a primary deformation twin interface. Figure 10 shows SADPs indexed as a $\{332\} < 113 >$ twin pattern, taken from the interface of a primary deformation twin. Figures 10 a), b) and c) present SADPs from the matrix, interface and twin crystals, respectively. In Figure 10 b), the twin axis and twin plane ($g = \{332\}_\beta$) are highlighted, as well as the outline of the projection of the reciprocal unit cell (first Brillouin Zone) of each crystal. Also of note in the two-beam BF image in Figure 10 d) is the high density of dislocations visible near the twinning interface. Although not shown here, this is a commonly observed feature in many $\{332\} < 113 >$ twins [31, 32] deformed at quasi-static strain rates and confirmed by TEM in this work.

# 5 Discussion

## 5.1 TWIP in BCC Versus FCC

It is well known that for TWIP face centered cubic (FCC) steels, the total contribution to plastic strain from deformation twinning is roughly on the order of 3-5 % [8]. Zhou et al. [27] and Min et al. [29, 30] found that $\{332\} < 113 >$ twins contribute much more to the total strain in TWIP Ti alloys, and that certain grains when oriented near the $[\bar{1}22]$ axis, could provide up to 80% of the plastic strain, as twin area fraction in these grains rapidly reaches 0.8. Although certain preferably oriented grains accommodate most of the plastic strain by $\{332\} < 113 >$ twinning, averaged over all measured grains, the twin area fraction reached a maximum of roughly 0.5. The higher twin fraction implies the total contribution of twinning in $\{332\} < 113 >$ TWIP $\beta$ Ti alloys is larger than in TWIP steels.

TWIP strongly affects the WHR, as shown in TWIP steels, through the so-called dynamic Hall-Petch effect, i.e., a dynamic refinement of the mean free path of dislocations. This appears to be the case in TWIP Ti alloys also. Min et al. were able to explain in large part the contribution of TWIP to the WHR using the dynamic Hall-Petch effect in Ti-15Mo [29]. Secondly, Min et al. and Zhou et al.'s study on Ti-15Mo [29, 30, 27] highlight how $\{332\} < 113 >$ twins seem to form by accommodating the imposed strain, not stress. Specifically, Min et al. [30] showed that on a grain by grain basis, twinning was almost completely absent in grains oriented preferentially for slip, even if the local stresses within those grains were high. This might explain the similarities between the stress-strain response of the Ti-15Mo specimens at $10^{-3}$ and $10^{-1}$ $s^{-1}$. This is further highlighted when the WHR is shown as a function of true stress (Figure 2 c), where it can be seen that the two curves overlap once the yield stress has been reached. In essence, Ti-15Mo exhibits similar work hardening for a similar flow stress, regardless of the strain rate at which it is deformed. Once the capacity for twinning is exhausted, the normal, decreasing

work hardening of slip-dominant deformation takes over. From this stage onward to fracture, the work hardening curves truly match up independent of strain rate, as would be expected for a slip-dominant BCC crystal. As such, it seems as though the ability to exhibit deformation twinning is exhausted over a smaller range of flow stresses, and lower absolute levels of plastic strain result as strain rate is increased.

In FCC crystals, the yield stress, in general, is not highly sensitive to strain rate or temperature, due to the mostly athermal barrier for slip. However, work hardening is highly temperature sensitive, as the stacking fault energy (SFE) decreases with temperature and cross-slip is discouraged. Difficult cross-slip leads to an increased back-stress on slip systems, promoting hardening and retarding dynamic recovery. It is well reported that low SFE FCC materials exhibit increased work hardening and ductility at reduced temperatures [33, 34]. Hence, in FCC TWIP steels, the low SFE and deformation twinning itself both contribute to increasing work hardening as thermal activation is reduced (either by reducing temperature or increasing strain rate).

When BCC TWIP Ti alloys are considered in the same light, the conclusion is less promising. The stress necessary for slip has a strong thermal component, due to the core structure of screw dislocations in BCC alloys [35, 36]. However, work hardening is not strongly dependent on strain rate. When the contribution of TWIP is considered, decreasing thermal activation from increased strain rates should theoretically cause only small differences in twinning activity, due to the athermal nature of the twinning stress [37, 38, 8]. However, the result is still an altogether reduced capacity to accumulate plastic deformation as strain rate increases (or temperature decreases), as the contribution to WHR from twinning stays relatively constant per plastic strain increment. The BCC structure of TWIP Ti alloys, compounded with reduced twinning activity at increased strain rates, makes TWIP Ti less promising for high strain rate applications.

## 5.2 TRIP Versus TWIP at High Strain Rates: Work Hardening and Strain Relaxation

Although we do not have comparable intermediate strain rate data available for TRIP/TWIP Ti-12Mo, we can turn to TRIP/TWIP Ti-10V-3Fe-3Al (wt.%) and TRIP Ti-10V-2Fe-3Al (wt.%) data available form Ahmed et al. and Ma et al., respectively, to understand the effect of increasing from quasi-static to intermediate strain rates on work hardening provide by TRIP [12, 13]. In both cases, the shape of the stress-strain response and resulting WHR is unchanged by increasing strain rate. Ma et al. reports the true strain at which yield and minimum WHR occur do not significantly change over 5 orders of magnitude of strain rate.

When the mechanical testing data presented in Figure 3 is considered, specifically comparing both alloys, it seems as though Ti-12Mo is more efficient at accommodating the imposed high strain rate deformation than Ti-15Mo. This is also supported by the x-ray imaging used to determine the reduction in width up to fracture, as shown in Figure 5. Both the mechanical testing data and x-ray imaging show that Ti-12Mo exhibits higher ductility at both strain rates compared to Ti-15Mo up to fracture. The increased ductility associated to TRIP also correlated with a more gradual rate of microstructural evolution as a function of strain (Figure 4 e) and f). Secondly, Ti-12Mo exhibits a larger increase in flow stress for the same increase in strain rate compared to Ti-15Mo, indicating that Ti-12Mo has a higher strain rate sensitivity (Figure 3). It also appears as though adiabatic heating does not have a significant effect on TRIP in Ti-12Mo, as discussed in the supplementary materials. A lower concentration of Mo leads to a less stable $\beta$-phase. Both alloys exhibit TWIP during deformation. However, Ti-12Mo also exhibits TRIP. In fact, when the results shown in Figure 7 are considered, it seems as though TRIP plus TWIP leads to the formation of a much finer microstructure than TWIP alone produces

in Ti-15Mo. The exact reasons for this are still unknown, but martensite appears to form sub-micron and even nanometer scale features that result in more efficient accommodation of local strains, which maintains hardening to higher strains.

As stated in recent studies on TRIP/TWIP $\beta$ Ti alloys [9, 11, 26], martensitic transformation seems to be an important mechanism for alleviating local stresses and elastic strains caused by concentrated microstructure evolution, specifically at the intersection of secondary and tertiary deformation products (Figure 6). TWIP in both alloys contributes to increasing the work hardening during plasticity, and the effects reported at quasi-static strain rates are still observed at higher strain rates. However, it seems that alleviating the local build-up of strain and resulting stress is a more prominent concern in TWIP BCC alloys deformed at higher strain rates. TRIP, on the other hand, serves to alleviate the local build-up of strain on the sub-micron scale in Ti-12Mo, which allows for refinement of the microstructure and dislocation density to increase before dynamic recovery, local strain, and stress cause localization and fracture.

One major caveat to consider is the absence of nanoscale twin structures in Ti-15Mo. Considering the evidence shown herein and by other quasi-static studies on Ti-12Mo and Ti-15Mo alloys [1, 11, 27, 29], Ti-12Mo is clearly able to form much finer microstructures during plastic deformation, even at higher strain rates. Recent publications on multi-modal TWIP alloys, where both $\{332\} < 113 >$ and $\{112\} < 111 >$ twinning modes are concurrently active, like Ti-7Mo-3Cr (wt. %) [39], Ti-4Mo-3Cr-1Fe (wt. %) [3], or Ti-Mo-Zr ternaries [40, 41], exhibit a structural refinement that is greater than found in Ti-15Mo. Testing multi-modal TWIP alloys at higher strain rates would help to shed light on the role of TWIP versus TRIP in work hardening versus strain relaxation.

# 6 Conclusions

We have used a combination of ultrafast synchrotron x-ray imaging and diffraction during high strain rate tensile testing and post-mortem characterization to compare and contrast the microstructure evolution of TRIP/TWIP Ti-12Mo and TWIP Ti-15Mo for the first time. These results provide key insights into the contributions of TRIP/TWIP for increased ductility in metastable Ti alloys during high strain rate deformation. The following conclusions can be drawn from this work:

- Quasi-static and intermediate strain rate tensile testing of TWIP Ti-15Mo showed that while TWIP contributes strongly to increasing work hardening, the intrinsic strain rate sensitivity of dislocations in the BCC crystal limit the maximum strength reached. For low to intermediate strain rates, once the contribution to work hardening from twinning is exhausted, slip takes over and the WHR curves overlap up to fracture, resulting in a severe reduction in elongation during tensile deformation with increasing strain rate.

- Ti-12Mo differs from Ti-15Mo during high strain rate testing, due to TRIP activation during deformation. TRIP has been shown to alleviate local elastic strain resulting from microstructure evolution during deformation. TWIP is still active as a primary and secondary deformation mechanism, however, in Ti-12Mo. The high strain rate mechanical testing data clearly shows that Ti-12Mo exhibits, on average, a higher total elongation at both strain rates.

- The activation of TRIP is believed to accommodate a portion of the imposed deformation and concurrently alleviates local strains from extensive twin formation. The combination of TRIP and TWIP appears to offer superior combinations of strength and ductility at high strain rates over TWIP alone for metastable Ti alloys.

This study shows that TRIP is crucial to maintaining high elongations during high strain rate mechanical testing compared to TWIP alone in metastable $\beta$ Ti

alloys. Implications of this study potentially shift the focus from TWIP-dominant alloys to optimized combinations of TRIP/TWIP for alloy, microstructure, and property design.

# 7 Aknowledgements

This work was supported by the department of the Navy, Office of Naval Research under award No. N00014-18-1-2567. Any opinions, findings, and conclusions or recommendations expressed in this material are those of the author(s) and do not necessarily reflect the views of the Office of Naval research. The authors gratefully acknowledge ATI Metals, a member of the Center for Advanced Non-Ferrous Structural Alloys (CANFSA), a National Science Foundation Industry/University Cooperative Research Center (I/UCRC) (Award No. 1624836) at the Colorado School of Mines, for providing the material studied in this manuscript.The authors gratefully acknowledge ATI (Allegheny Technologies Incorporated) for providing the Ti-15Mo studied in this work. The authors also thank the Center for Advanced Non-Ferrous Structural Alloys (CANFSA), a National Science Foundation Industry/University Cooperative Research Center (I/UCRC) [Award No. 2137243] at the Colorado School of Mines for support during the preparation of this manuscript. This research used resources of the Advanced Photon Source, a US Department of Energy (DOE) Office of Science User Facility operated for the Office of Science by Argonne National Laboratory under contract no. DE-AC02-06CH11357. We also gratefully acknowledge the help of D. Hammond (Mines) with selected measurements of imaging data.

# 8 Declaration of Competing Interests

The authors have no competing interests to declare.

# 9 Data Availibility

The Authors will make data available upon reasonable request.

# References


[1] Marteleur M, Sun F, Gloriant T, Vermaut P, Jacques PJ, Prima F. On the design of new $\beta$-metastable titanium alloys with improved work hardening rate thanks to simultaneous TRIP and TWIP effects. Scripta Materialia. 2012;66(10):749–752.

[2] Brozek C, Sun F, Vermaut P, Millet Y, Lenain A, Embury D, et al. A $\beta$-titanium alloy with extra high strain-hardening rate: design and mechanical properties. Scripta Materialia. 2016;114:60–64.

[3] Ren L, Xiao W, Ma C, Zheng R, Zhou L. Development of a high strength and high ductility near $\beta$-Ti alloy with twinning induced plasticity effect. Scripta Materialia. 2018;156:47–50.

[4] Danard Y, Lilensten L, Sun F, Vermaut P, Von Thüngen IF, Martin G, et al. Strain-hardenability of new strengthened TRIP/TWIP titanium alloys. In: MATEC Web of Conferences. vol. 321. EDP Sciences; 2020. p. 11056.

[5] Hanada S, Yoshio T, Izumi O. Effect of plastic deformation modes on tensile properties of beta titanium alloys. Transactions of the Japan institute of metals. 1986;27(7):496–503.

[6] Castany P, Gloriant T, Sun F, Prima F. Design of strain-transformable titanium alloys. Comptes Rendus Physique. 2018;19(8):710–720.

[7] Matlock DK, Speer JG, De Moor E, Gibbs PJ. Recent developments in advanced high strength sheet steels for automotive applications: an overview. Jestech. 2012;15(1):1–12.

[8] De Cooman BC, Estrin Y, Kim SK. Twinning-induced plasticity (TWIP) steels. Acta Materialia. 2018;142:283–362.

[9] Danard Y, Poulain R, Garcia M, Guillou R, Thiaudière D, Mantri S, et al. Microstructure Design and in-situ investigation of TRIP/TWIP effects in a forged dual-phase Ti–10V–2Fe–3Al alloy. Materialia. 2019:100507.

[10] Bingnan Q, Fan S, VERMAUT P, PRIMA F. Fine-tuning of stress-induced martensite in TRIP/TWIP Ti alloys. In: MATEC Web of Conferences. vol. 321. EDP Sciences; 2020. p. 11038.

[11] Zhang J, Li J, Chen Z, Meng Q, Sun F, Shen B. Microstructural evolution of a ductile metastable $\beta$ titanium alloy with combined TRIP/TWIP effects. Journal of Alloys and Compounds. 2017;699:775–782.

[12] Ahmed M, Wexler D, Casillas G, Savvakin DG, Pereloma EV. Strain rate dependence of deformation-induced transformation and twinning in a metastable titanium alloy. Acta Materialia. 2016;104:190–200.

[13] Ma X, Li F, Cao J, Li J, Sun Z, Zhu G, et al. Strain rate effects on tensile deformation behaviors of Ti-10V-2Fe-3Al alloy undergoing stress-induced martensitic transformation. Materials Science and Engineering: A. 2018;710:1–9.

[14] Sadeghpour S, Javaheri V, Bruschi S, Kömi J, Karjalainen P. Strain rate and mechanical stability in determining deformation behavior of beta Ti alloys. Materials Science and Engineering: A. 2020;798:140274.

[15] Meyers MA. Dynamic behavior of materials. John wiley & sons; 1994.

[16] Yang H, Wang D, Zhu X, Fan Q. Dynamic compression-induced twins and martensite and their combined effects on the adiabatic shear behavior in a Ti-8.5 Cr-1.5 Sn alloy. Materials Science and Engineering: A. 2019;759:203–209.

[17] Xiao J, Nie Z, Tan C, Zhou G, Chen R, Li M, et al. The dynamic response of the metastable $\beta$ titanium alloy Ti-2Al-9.2 Mo-2Fe at ambient temperature. Materials Science and Engineering: A. 2019;751:191–200.

[18] Wang Y, Liu X, Im KS, Lee WK, Wang J, Fezzaa K, et al. Ultrafast X-ray study of dense-liquid-jet flow dynamics using structure-tracking velocimetry. Nature Physics. 2008;4(4):305–309.

[19] Hudspeth M, Claus B, Dubelman S, Black J, Mondal A, Parab N, et al. High speed synchrotron x-ray phase contrast imaging of dynamic material response to split Hopkinson bar loading. Review of Scientific Instruments. 2013;84(2):025102.

[20] Hudspeth M, Sun T, Parab N, Guo Z, Fezzaa K, Luo S, et al. Simultaneous X-ray diffraction and phase-contrast imaging for investigating material deformation mechanisms during high-rate loading. Journal of Synchrotron Radiation. 2015 Jan;22(1):49–58.

[21] Sun T, Fezzaa K. HiSPoD: a program for high-speed polychromatic X-ray diffraction experiments and data analysis on polycrystalline samples. Journal of synchrotron radiation. 2016;23(4):1046–1053.

[22] Standard A. E8. Standard test method for tension testing of metallic materials. West Conshohocken (USA): ASTM. 2004.

[23] Zhao GH, Xu X, Dye D, Rivera-Díaz-del Castillo PE. Microstructural evolution and strain-hardening in TWIP Ti alloys. Acta Materialia. 2020;183:155–164.

[24] Sun F, Zhang J, Vermaut P, Choudhuri D, Alam T, Mantri S, et al. Strengthening strategy for a ductile metastable $\beta$-titanium alloy using low-temperature aging. Materials Research Letters. 2017;5(8):547–553.

[25] Xiao JF, Nie ZH, Tan CW, Zhou G, Chen R, Li MR, et al. Effect of reverse -to- transformation on twinning and martensitic transformation in a metastable titanium alloy. Materials Science and Engineering: A. 2019;759:680 – 687.

[26] Lilensten L, Danard Y, Brozek C, Mantri S, Castany P, Gloriant T, et al. On the heterogeneous nature of deformation in a strain-transformable beta metastable Ti-V-Cr-Al alloy. Acta Materialia. 2019;162:268–276.

[27] Zhou X, a Min X, Emura S, Tsuchiya K. Accommodative {332}< 113> primary and secondary twinning in a slightly deformed $\beta$-type Ti-Mo titanium alloy. Materials Science and Engineering: A. 2017;684:456–465.

[28] Lin F, Marteleur M, Jacques PJ, Delannay L. Transmission of 332[U+3008]113[U+3009] twins across grain boundaries in a metastable - titanium alloy. International Journal of Plasticity. 2018;105:195–210.

[29] Min X, Chen X, Emura S, Tsuchiya K. Mechanism of twinning-induced plasticity in $\beta$-type Ti-15Mo alloy. Scripta Materialia. 2013;69(5):393–396.

[30] Min X, Emura S, Chen X, Zhou X, Tsuzaki K, Tsuchiya K. Deformation microstructural evolution and strain hardening of differently oriented grains in twinning-induced plasticity titanium alloy. Materials Science and Engineering: A. 2016;659:1–11.

[31] Hanada S, Ozeki M, Izumi O. Deformation characteristics in $\beta$ phase Ti-Nb alloys. Metallurgical transactions A. 1985;16(5):789–795.

[32] Hanada S, Izumi O. Transmission electron microscopic observations of mechanical twinning in metastable beta titanium alloys. Metallurgical Transactions A. 1986;17(8):1409–1420.

[33] Carreker Jr R, Hibbard Jr W. Tensile deformation of high-purity copper as a function of temperature, strain rate, and grain size. Acta Metallurgica. 1953;1(6):654–663.

[34] Carreker R. Tensile deformation of silver as a function of temperature, strain rate, and grain size. Jom. 1957;9(1):112–115.

[35] Dieter GE, Bacon DJ. Mechanical metallurgy. vol. 3. McGraw-hill New York; 1986.

[36] Hull D, Bacon DJ. Introduction to dislocations. Butterworth-Heinemann; 2001.

[37] Meyers M, Vöhringer O, Lubarda V. The onset of twinning in metals: a constitutive description. Acta materialia. 2001;49(19):4025–4039.

[38] Gray III GT. High-strain-rate deformation: mechanical behavior and deformation substructures induced. Annual Review of Materials Research. 2012;42:285–303.

[39] Gao J, Huang Y, Guan D, Knowles AJ, Ma L, Dye D, et al. Deformation mechanisms in a metastable beta titanium twinning induced plasticity alloy with high yield strength and high strain hardening rate. Acta Materialia. 2018;152:301–314.

[40] Zhang J, Li J, Chen G, Liu L, Chen Z, Meng Q, et al. Fabrication and characterization of a novel $\beta$ metastable Ti-Mo-Zr alloy with large ductility and improved yield strength. Materials Characterization. 2018;139:421–427.

[41] Zhang J, Fu Y, Wu Y, Qian B, Chen Z, Inoue A, et al. Hierarchical $\{332\}<113>$ twinning in a metastable $\beta$ Ti-alloy showing tolerance to strain localization. Materials Research Letters. 2020;8(7):247–253.

[42] Bergman TL, Incropera FP, Lavine AS, Dewitt DP. Introduction to heat transfer. John Wiley & Sons; 2011.

[43] Hecker S, Stout M, Staudhammer K, Smith J. Effects of strain state and strain rate on deformation-induced transformation in 304 stainless steel: Part I. Magnetic measurements and mechanical behavior. Metallurgical Transactions A. 1982;13(4):619–626.

[44] Finfrock CB, Thrun MM, Bhattacharya D, Ballard TJ, Clarke AJ, Clarke KD. Strain rate dependent ductility and strain hardening in Q&P steels. Metallurgical and Materials Transactions A. 2021;52(3):928–942.

# 10 Supplementary Materials

## 10.1 Mechanical Discussion

According to Meyers [15], Kolsky pressure bar equations to obtain the strain rate and strain signal from strain gauge data are as follows:

$$\dot{\varepsilon}(t) = -\frac{2C_0}{L}\varepsilon_R(t) \tag{1}$$

$$\varepsilon(t) = -\frac{2C_0}{L}\int \varepsilon_R(t)dt \tag{2}$$

where $C_0$ is the speed of sound in the incident bar, L is the length of the sample and $\varepsilon_R(t)$ is the amplitude of the reflected pulse as a function of time. These two equations allow for the calculation of the "imposed strain" signal acting on the mobile side of the bar setup, i.e., analogous to the crosshead in a conventional load frame. Typical examples of strain versus time signal are shown in Figure 11 c). For both strain rates, the rise time of the load pulse is roughly 50-60 $\mu s$, which corresponds to roughly 0.02 imposed strain. This implies that the sample has not reached a constant velocity until this strain level has been reached, and should be kept in mind when interpreting the mechanical property results.

In a conventional Split-Hopkinson bar setup, the fixed-side of the sample would be attached to an additional slender bar for measuring the transmitted stain pulse and stress measurements. In our case, the size limitation of the hutch at the beamline imposed the use of a load cell instead. Load cells directly convert voltage to newtons, such that the signal need only be divided by the area of the specimen gauge section ($A_s$):

$$\sigma(t) = \frac{F(t)}{A_s} \tag{3}$$

In our case, because we use a load cell instead of a transmission bar, this side

is assumed to be an "anvil", and thus a fixed boundary with an infinite impedance. For this assumption to be valid, it implies that the stress pulse undergoes perfect reflection upon reaching the fixed end. The boundary conditions for reflection of a stress wave against a rigid body are that the particle velocity must remain 0 in the rigid body, while the reflected pulse and stress will be equal in magnitude and sign to that of the incident pulse [15]. In this work, the reflected pulse has important variations in the plateau region, leading to the conclusion that motion was transmitted to the load cell. This implies that the fixed boundary condition assumption was not fully achieved.

Another aspect to consider is the intrinsic impedance of the samples which is higher than that of the incident bar. As per Meyers [15], when a stress wave arrives at an interface, equilibrium of forces and velocities must be maintained:

$$\sigma_I A_0 + \sigma_R A_0 = \sigma_T A_s \tag{4}$$

and

$$U_{0I} + U_{0R} = U_{sT} \tag{5}$$

where $\sigma$ denotes stress, A denotes area, and U denotes particle velocity. Subscripts I, R and T represent the incident, reflected and transmitted components, and subscript 0 and s refer to the incident bar and the sample, respectively. Knowing that:

$$\sigma = \rho \frac{dx}{dt} U \tag{6}$$

and, in a slender bar, where lateral confinement is absent and dispersion is neglected:

$$\frac{dx}{dt} = V_{long} = C = \sqrt{\frac{E}{\rho}} \tag{7}$$

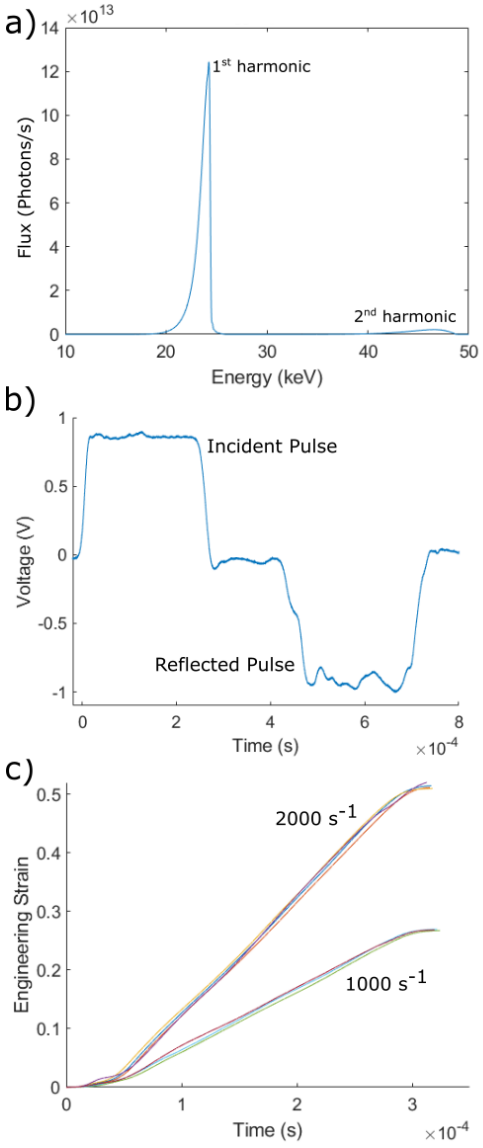


**Figure 11:** a) Energy spectrum for the pink beam used for in-situ synchrotron imaging and diffraction. b) Raw voltage versus time profile of the strain gauge signal for a typical test, showing the incident and reflected pulses. c) Integrated reflected pulse signal, showing strain versus time for both strain rates used in the high strain rate modified (Kolsky) pressure bar experiments.

Such that for an Al incident bar, $C_0 = 5051\ ms^{-1}$ ($C_0 = 5091\ ms^{-1}$ measured), for a $\beta$ phase Ti sample $E = 80\ GPa$, and $\rho = 5199\ kg/m^3$ and $\rho = 5372\ kg/m^3$ for Ti-12Mo and Ti-15Mo, respectively. Taking an average density of $\rho = 5280\ kg/m^3$, the velocity of a longitudinal wave is $C_s = 3891\ m/s$. The impedances (or the product $\rho C$) of the incident bar and the sample are thus $1.437 \times 10^7\ kg/m^2s$ and $2.07 \times 10^7\ kg/m^2s$, respectively. The cross-sectional area of each also acts as a

geometric impedance. Using equations 4 and 5, it can be shown that:

$$\frac{\sigma_R}{\sigma_I} = \frac{A_0\rho_0C_0 - A_s\rho_sC_s}{A_s\rho_sC_s + A_0\rho_0C_0} \tag{8}$$

The area of the incident bar is 126 $mm^2$ and the cross-section of the gauge of the specimens is 0.5 $mm^2$. Unsurprisingly, when the contribution of geometry is considered, the ratio $\sigma_R/\sigma_I$ is close to unity, because the total impedance of the sample is low relative to that of the incident bar. As such, assuming the sample has a negligible total impedance relative to the incident bar is reasonable. To support this assumption, Figure 11 b) shows the magnitude and duration of the reflected pulse is similar to the incident pulse (neglecting the apparent wave dispersion).

Lastly, it should be stated that at least 3 reverberations are necessary to obtain a state of homogeneous stress in the sample [15]. Considering the velocity of a longitudinal elastic wave in the sample is $C_s = 3891\ ms^{-1}$ and 3 times the gauge length is equal to 12 $mm$, roughly 3 $\mu s$ are necessary for a homogeneous state of stress to arise in the sample.

These discussion points ultimately show that many of the assumptions used in the stress-strain analysis of a "Split-Hopkinson pressure bar" type of setup are respected. First, seeing as how the pulse length relative to the duration of the test is high and the sample impedance is negligible relative to that of the bar and anvil, little energy loss is exhibited by the elastic pulse as it deforms the sample and is reflected, meaning that negligible acceleration is felt by the bar during the test. In fact, most of the deviation exhibited seems to be the result of motion within the load cell on the anvil side and slack in the threads during loading. Coupled to the relatively rapid rise time and short time required to establish a homogeneous stress state in the gauge length implies the assumption of a constant strain rate uniaxial tensile stress state is acceptable (at least from 2% strain to fracture). Indeed, it seems that most of the artifacts in the mechanical testing data may arise from the

compliance of the load cell.

## 10.2 The Role of Adiabatic Heating on TRIP

Heat accumulation from plastic work becomes a concern when the characteristic time for the deformation event to occur becomes smaller than the time for the generated heat to diffuse away from the sample. This condition can be considered as quasi-adiabatic, wherein the event can be considered to occur in the absence of heat transfer to the environment. A useful equation for determining the threshold is the characteristic diffusion distance for a given time:

$$d_t = 1.2\sqrt{(\alpha t)} \tag{9}$$

where :

$$\alpha = \frac{k}{\rho c_p} \tag{10}$$

where $\alpha$ is thermal diffusivity, $d_t$ is the characteristic diffusion distance, t is time (equivalent to strain rate in this case), and k is thermal conductivity, $\rho$ is density and $c_p$ is specific heat. Typical values for $\beta$ Ti alloys were used for these calculations, including: $k = 7.8\ W/mK$, $\rho = 5285\ kg/m^3$ (average density for T-12Mo and Ti-15Mo), $c_p = 525\ J/kgK$. These parameters give a thermal diffusivity $\alpha = 2.81 \times 10^{-6}$ $m^2/s$, which is almost an order of magnitude lower than mild steel ($\alpha = 18.8 \times 10^{-6}$ $m^2/s$) and is still lower than that of 304 stainless steel ($\alpha = 3.5 \times 10^{-6}\ m^2/s$) [42]. As expected, this results in quasi-adiabatic conditions being reached at lower strain rates than for a mild steel sample (AISI 1010) of the same dimensions (Figure 12). The two horizontal lines in Figure 12 represent the thickness of the gauge section for the intermediate strain rate tensile specimens (6.35 $mm$) and the high strain rate (in-situ) tensile specimens (0.5 $mm$).

Adiabatic heating has been found to be an important consideration in the strain

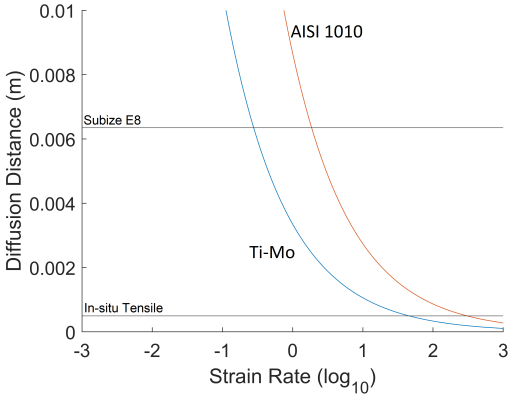


**Figure 12:** Characteristic thermal diffusion distance versus strain rate for averaged Ti-Mo composition, equivalent to Ti-13.5Mo (wt %) and AISI 1010 mild steel.

rate sensitivity of TRIP in steels [43, 44], which stems from the thermodynamics of TRIP. In general, The higher the testing temperature, the lower the undercooling relative to $M_s$, and more mechanical energy is needed to to drive the transformation.

If it is known that quasi-adiabatic conditions subsist during testing and calculating the temperature rise induced during testing is a matter of calculating the plastic work produced during the deformation and converting that energy to heat. As such, integrating the area under the true stress versus true strain curve gives the total temperature rise as follows:

$$\Delta T = \beta \int \frac{\sigma(\varepsilon) d\varepsilon}{\rho c_p} \tag{11}$$

where $\beta$ is the fraction of work converted to heat, taken as 0.9 here, and $\sigma(\varepsilon)$ is the true stress response as a function of true strain. As discussed previously, the mechanical data available from high strain rate testing is highly variable. Thus, using the stress-strain data to calculate an exact temperature rise versus strain would lead to large uncertainty. However, the calculated values are a useful estimate for the purpose of discussion. The calculated total values vary between 25 and 35 K for both alloys at both strain rates. This temperature rise is also considered as a high-end conservative estimate, as the entire stress-strain curve was used for integration, which includes any post-uniform elongation that occurred.

A total temperature rise of roughly 30 K is not considered to have a large effect on TRIP and martensite undercooling. This value is comparatively small, due to Ti's low density and specific heat. The product of the two quantities ($\rho c_p$) gives a relative indication of the temperature rise obtained for an increment of plastic work. This parameter is 40% higher in steels, which helps to explain why adiabatic heating may be a more important factor in the strain rate sensitivity of TRIP steels [44]. Lastly, it should also be noted that the temperature dependence of TRIP stress in Ti alloys is still not well understood. The presence of athermal $\omega$ phase in the undeformed state competes with deformation-induced martensite and adds a degree of freedom in determining the mechanical component of the free energy for transformation.

## 10.3 Secondary Twinning in TWIP Ti-15Mo

Figure 13 a) shows an IPF + IQ map with twinning boundaries overlaid and Figure 13 b) shows a representative schematic of the band in the region enclosed by the dashed circle in a). The schematic clearly shows that $\{112\} < 111 >$ twin boundaries are only present when two variants of the secondary $\{332\} < 113 >$ intersect. Figure 13 c) shows a misorientation profile for the line indicated by an arrow and labeled 1 in a). This line profile indicates that each of these parallel secondary twin boundaries present a misorientation characteristic of a $\{332\} < 113 >$ twin. On the other hand, the misorientation line profile indicated by the arrow labeled 2 was chosen to intersect both $\{332\} < 113 >$ and $\{112\} < 111 >$ boundaries. Indeed, Figure 13 d) shows that the misorientations of 50.5° and 60° are measured where the $\{332\} < 113 >$ and $\{112\} < 111 >$ twin boundaries are expected, further supporting this finding.

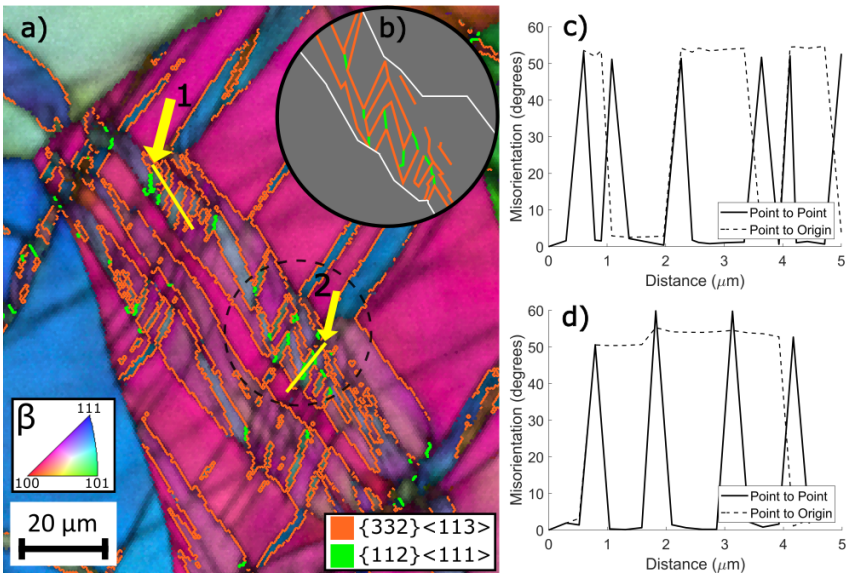


**Figure 13:** Detailed IPF map, highlighting the secondary twinning structure in Ti-15Mo. a) IPF + IQ map. Twin boundaries are also overlaid: orange represents $\{332\} < 113 >$ twin boundaries, while green represents $\{112\} < 111 >$ twin boundaries. Yellow arrows labeled 1 and 2 point to line profiles shown in c) and d), respectively. b) Schematic of secondary boundaries contained within the larger primary twin. The region the schematic is indicated by the dashed circle in a). The color scheme for boundaries is the same as in a). c) Misorientation profile for the line indicated at 1 in a). d) Misorientation profile for the line indicated at 2 in a)